Composites: Part A 143 (2021) 106281

Contents lists available at ScienceDirect

Composites Part A

journal homepage: www.elsevier.com/locate/compositesa

An evaluation of the influence of manufacturing methods on interlocked aluminium-thermoplastic composite joint performance

Karthik Ramaswamy, Ronan M. O'Higgins *, John Lyons, Michael A. McCarthy, Conor T. McCarthy

CONFIRM Centre and Bernal Institute, University of Limerick, Ireland

ARTICLE INFO

Keywords:
A. Discontinuous reinforcements
D. Mechanical testing
D. Fractography
E. Joints/joining
Hybrid joints

ABSTRACT

Joining techniques for multi-material structures are critical for increased use of lightweight materials such as aluminium alloys and thermoplastic composites in the automotive industry. Interlocking adhesive joints (IAJs) can provide increased mechanical performance over standard adhesive joints, but manufacturing methods suitable for industrial applications must be developed. Here, three methods are examined for fabricating composite adherends with recessed macroscale features. The methods differ in the way the fabric material is draped over a mould and are referred to as "simple-stacking", "moulding-in", and "fibre-cutting". The IAJs are tested under quasi-static, 0.5 m/s and 3 m/s loading rates and the fibre-cutting method achieves the best mechanical performance. One reason is that it gives a homogenous fibre distribution across the overlap width, providing good flexural properties at the recessed features. It also results in resin-rich regions along the overlap length, which lead to beneficial "snubbing" for improved interlocking, and progressive, energy-absorbing failure. The fibre-cutting method is simple to automate and well-suited for scale-up to industrial manufacturing.

1. Introduction

Statutory requirements on emissions, fuel efficiency, and crashworthiness call for the development of light-weight, crashworthy automotive structures [1,2]. Electric vehicles also demand light-weight structures to compensate for the weight of the batteries and electric drivetrain [3,4]. These considerations are driving increased use of carbon fibre-reinforced plastic (CFRP) composites, with thermoplastic composites being of particular interest due to their short processing cycles, high fracture toughness, unlimited shelf-life, good solvent resistance, and inherent recyclability. Since all-composite structures are currently too expensive for production vehicles, multi-material structures involving thermoplastic CFRP composites and aluminium alloys offer the most attractive solution for light-weighting and crashworthiness. However, joining low surface energy thermoplastic matrix composites to aluminium alloys presents a considerable challenge.

Mechanical fastening, although widely used, is detrimental for mechanical properties of notch-sensitive composites and can be susceptible to galvanic corrosion depending on the material combination used. Adhesive joining presents challenges such as brittle failure, poor damage tolerance and environmental ageing. Laminated composites in particular, are susceptible to delamination due to the high peel stress that occurs in bonded joints, which loads the laminate in its weakest through-thickness direction. New joining techniques are desirable to improve the damage tolerance of bonded/co-cured metal-composite joints. Through-thickness reinforced (TTR) joining techniques attempt to address these issues using arrays of interlocking protrusions and cavities on the faying surfaces of adherends. Table 1 summarises previous TTR joining studies and detailed reviews are presented in [5–7]. As can be seen, most studies have employed thermoset composites co-cured to steel or titanium. Relatively few have studied aluminium/composite joints [8–12]. Graham et al. [9] employed cold-metal transfer (CMT)-welded pins, reporting that the pins were susceptible to shearing at the base, which limited joint performance. It was suggested that the optimisation of pin geometry could improve performance.

TTR metal-composite joining is a two-step process. The first step involves surface structuring of the metal adherend using either advanced techniques like additive manufacturing and electron beam machining or simple drilling and insertion of pins. In the second step, layers of non-crimp fabric, woven fabric or uncured prepreg plies are manually pressed around the metal protrusions, in as uniform manner as possible. Given the large number and small size of the protrusions

* Corresponding author.
E-mail address: ronan.ohiggins@ul.ie (R.M. O'Higgins).

https://doi.org/10.1016/j.compositesa.2021.106281
Received 9 August 2020; Received in revised form 7 December 2020; Accepted 10 January 2021
Available online 17 January 2021

Table 1
Through-thickness reinforced hybrid metal-composite joint studies.

Authors	Surface structuring	Joint type*	Adherend materials	Joining process
Smith et al. (2005) [13]	Electron-beam (Surfisculpt™)	DLJ	- Stainless-steel (AISI 316L) - GFRP (plain woven E-glass fabric/polyester)	Co-curing (resin infusion)
Ucsnik et al. (2010) [14]	Cold-metal transfer	DLJ	- Stainless-steel (DIN1 3401) - CFRP (biaxial non-crimp fabric/epoxy)	Co-curing (vacuum-assisted resin infusion)
Parkes et al. (2014) [15]	Additive manufacturing (direct laser sintering)	SLJ	- Titanium (Ti–6Al–4 V) - CFRP (UD carbon fibre/ epoxy prepreg)	Co-curing (autoclave)
Graham et al. (2014) [9]	Additive manufacturing (laser metal deposition)	DLJ	- Stainless-steel (AISI 316L) - GFRP (plain woven glass/ epoxy)	Co-curing (vacuum-assisted resin transfer moulding)
	Cold-metal transfer	SLJ	- Mild-steel (ABS DH36) - GFRP (knitted E-glass/ vinylester) - Pins (AISI 316L)	Co-curing (vacuum-assisted resin transfer moulding)
	Cold-metal transfer	SLJ	- Titanium (Ti–6Al–4 V) - CFRP (UD carbon fibre/ epoxy prepreg)	Co-curing (autoclave)
	Cold-metal transfer	SLJ	- Aluminium (AA7050) - CFRP (UD carbon fibre/ epoxy prepreg)	Co-curing (autoclave)
	Capacitor discharge stud welding	SLJ	- Stainless steel (AISI 316L) - GFRP (plain-woven glass/ epoxy)	Co-curing (vacuum-assisted resin transfer moulding)
Xiong et al. (2015) [16]	Electron-beam (Surfisculpt™)	SLJ	- Titanium (Ti–6Al–4 V) - CFRP (plain woven carbon/ epoxy prepreg)	Co-curing (vacuum-assisted hot plate)
Islam et al. (2016) [17]	Z-pinning	SLJ	- Mild- carbon steel (A36) - GFRP (woven E-glass/epoxy prepreg) - Pins (stainless-steel pins)	Co-curing (hot press)
Wang et al. (2016) [18]	Electron-beam (Surfisculpt™)	DLJ	- Titanium (Ti–6Al–4V) - CFRP (UD carbon fibre/ epoxy prepreg)	Co-curing (autoclave)
Tang et al. (2018) [10]	Z-pinning	SLJ	- Aluminium (AA2024-T3) - CFRP (UD carbon fibre/ epoxy prepreg) - Pins (galvanised iron wire)	Secondary adhesive bonding
Fawcett et al. (2019) [8]	Cold working	SLJ	- Aluminium (AA2024-T3) - GFRP (8 harness satin woven E-glass/epoxy)	Co-curing (autoclave)
Abe et al. (2019) [11]	Chemical etching	SLJ	- Aluminium (AA5052) - CFRP (plain woven carbon/ polyamide 6)	Co-curing (hot press)
Rezvaninasab et al. (2019) [12]	Z-pinning	SLJ	- Aluminium (AA7075-T6) - GFRP (woven E-glass/epoxy) - Pins (high carbon and chromium steel)	Secondary adhesive bonding
Feistauer et al. (2020) [19]	U-joining	SLJ	- Titanium (Ti–6Al–4 V) - GFRP (glass/ polyetherimide)	Ultrasonic welding

* DLJ – double-lap joint, SLJ – single-lap joint.

(typically less than 1.5 mm in diameter), this step is suitable for low production volumes, but may not be feasible for integration into high productivity processes like stamp forming or compression moulding. From Table 1, for co-curing the assembled adherends, most studies employ resin infusion for dry fabrics and autoclaving for prepreg. In a recent review [7], co-curing was identified as the biggest obstacle for transitioning this technology from the laboratory to industrial applications, and the desirability of developing a simple, controlled process where the components are joined *after* curing, was highlighted. Another recent review [20], concluded that TTR is the most effective technique for increasing the strength of single-lap joints (SLJs), but also highlighted the manufacturing difficulty.

In the current work, manufacturing techniques for interlocking adhesive joints (IAJs), shown in Fig. 1, are studied. This IAJ design employs larger-scale protrusions than is typical in previous TTR methods, and has been shown in [21] to provide increased lap-shear strength (LSS) and work to failure (WF) compared to baseline adhesive joints (BAJs). In line with the recommendation in [7], the methods investigated are aimed at developing a simple, controlled process where the components are joined after curing. Macro-scale features are created on the faying surfaces of aluminium alloy and carbon-fibre-reinforced polyamide thermoplastic composite adherends, followed by bonding using a crash-durable epoxy adhesive. Three methods for fabricating composite adherends with recessed macro-scale features are investigated. All involve draping composite fabric preform over a mould with the desired features, followed by autoclaving. In method 1, the preform is simply stacked on top of the mould, in method 2 the fabric fibres are re-arranged around the mould features, and in method 3, warp yarns are selectively cut resulting in a hybridised discontinuous-fibre/woven-fabric in the vicinity of the features. The manufactured IAJs are tested under quasi-static and dynamic loading, since automotive structures must perform at crash loading rates, as well as normal, in-service loading rates. Deformation mechanisms and post-failure surfaces are analysed at macro and micro scales, and LSS, WF and ease of manufacture are evaluated. Results for BAJs are also given for comparison.

2. Materials and methods

2.1. Materials

A structural Al-Mg alloy, AA5754-H111 (Aalco Metals Ltd., 2018), employed in the automotive industry for its good corrosion resistance and formability, as well as moderate strength and weldability, is selected for the metallic adherends. The selected composite material is a 2/2 twill weave fabric preform (See Table 2). in which the fibres, consisting of carbon fibre cores, co-wrapped with Polyamide12 (PA12), are stretch-broken for high drapability (Schappe Techniques, France). The length of the stretch-broken carbon fibre (SBCF) is, on an average, 80 mm,

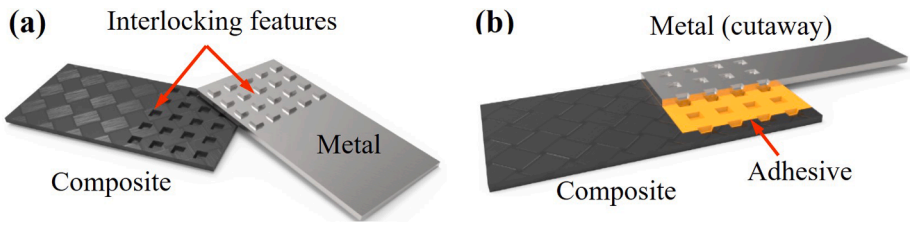

Fig. 1. Interlocking adhesive joint (IAJ): (a) composite and metal adherends with interlocking profiles, and (b) assembled joint (exploded section-view). (For interpretation of the references to colour in this figure legend, the reader is referred to the web version of this article.)

Table 2
Specifications of the carbon fibre reinforced thermoplastic composite.

Material supplier	Matrix polymer	Fibre type	Weaving pattern	Fibre volume fraction	Density	Nominal consolidated ply thickness
Schappe Techniques, France	Polyamide12 (PA12)	Teijin STS40 F11, Stretch-broken, 80 mm average fibre length	Co-wrapped 2/2 twill weave	52 ± 3%	1550 kg/m^3	0.27 mm

resulting in a high length-to-diameter aspect ratio. A stretch-broken textile composite allows realigning of the fabric yarns around the interlocking features. A polyamide 12 (PA12) matrix is chosen for its superiority over polypropylene (PP) and polyethene (PE) in terms of strength and stiffness, as well as adequate ductility, flexibility, and high-temperature performance. McDonnell et al. [22] compared the basic mechanical properties of the SBCF/PA12 material woven as 5-harness satin (5HS) fabric (Schappe Techniques) and the other commercially available, equivalent thermoplastic (polyetherimide, polyamide 66, PA12) and thermoset (epoxy) composite materials. The 5HS SBCF/PA12 material exhibited excellent tensile properties and mode I fracture toughness, comparable flexural properties, and relatively lower compression strength. The chosen 2/2 twill weave SBCF/PA12 fabric exhibits comparable tensile, compressive and flexural properties and significantly better shear properties relative to 5HS SBCF/PA12 fabric, which is not commercially available. Commingled/co-wrapped yarns offer the potential for low-cost manufacturing of complex-shaped composite parts and this chosen composite material system has been successfully investigated for compression moulding [22] and non-isothermal stamp forming [23]. The properties of this composite material make it attractive for use in the automotive industry. Table 3 summarises the mechanical properties of the adherend materials, provided by their respective suppliers. A one-component structural epoxy adhesive, Betamate 1496 V (Dow Automotive, USA, 2017), employed in the automotive industry to bond body panels, is used here due to its high stiffness and crash performance.

2.2. Single lap joint configuration and adherend manufacture

The single-lap joint (SLJ) specimen, illustrated in Fig. 2(a), has an overlap length of 25 mm, in accordance with ASTM D 5868 [24]. A grip-to-grip length of 150 mm was chosen to accommodate the slack

Table 3
Mechanical properties of the adherend materials.

AA5754-H111		**CF/PA12**			
Tensile modulus (GPa)	Tensile yield strength (MPa)	Warp tensile modulus (GPa)	Warp tensile strength (MPa)	Weft tensile modulus (MPa)	Weft tensile strength (MPa)
68	115	56	688	55	627
Ultimate tensile strength (MPa)	Strength coefficient (MPa)	Shear modulus (GPa)	Shear strength (MPa)	Flexural modulus (GPa)	Flexural strength (MPa)
299.6	469.4	5.5	113	49.5	636

mechanism in the high-speed testing machine [25]. To reduce the asymmetric stress distribution across the overlap caused by the dissimilar adherend materials, as recommended in [26], the adherend thicknesses were selected to balance the longitudinal and bending stiffnesses of the adherends relative to one another, as much as possible. Two SLJ configurations were investigated, namely: (i) the baseline adhesive joint (BAJ), with flat faying surfaces, and (ii) the IAJ. The IAJ design, Fig. 2 (b), was adapted from reference [27], and incorporates an array of truncated rectangular pyramid-shaped depressions on the faying surface of the composite adherend and corresponding projections on the aluminium adherend. The selected adherend thicknesses were considered as a design constraint in reference [27], therefore, any modification that demands change in the adherend thicknesses to ensure the stiffness balance is kept out-of-the-scope of this study. A constant bond line thickness of 0.25 mm was accounted for in the dimensions of the aluminium adherend. To minimise secondary bending due to loading eccentricity, 2 mm thick aluminium spacers were bonded to the adherends, see Fig. 2(a). In addition, to improve specimen gripping in the high-speed test machine, 0.25 mm thick aluminium tabs were also bonded to the adherends.

The metal adherends were machined from a 4 mm thick aluminium sheet, with a tolerance of ± 0.025 mm for all dimensions. For the composite adherends, a mould-tool with male interlocking features, capable of accommodating five composite adherends, Fig. 3(a), was manufactured through precision milling. The laminate consisted of 8 plies of fabric (0°, 90°) preform, and had a nominal thickness of 2.16 mm.

Three methods were employed for manufacturing the composite adherends, as illustrated in Fig. 3(b). The methods, together with their rank in terms of ease of manufacture are:

Method M1 – "Simple-stacking" (Rank 1): Here, the fabric plies were stacked on the mould-tool for consolidation in the autoclave. This method doesn't involve any additional operation and could be straightforwardly integrated into production, making it the easiest manufacturing method.

Method M2 – "Moulding-in" (Rank 3): This method has been inspired by work on moulding-in around bolts and pins which has been shown to result in higher strength joints compared to drilled specimens [28–30]. Here, the method involved a pre-forming operation where the commingled fabric yarns were rearranged around the features in the mould-tool. Seven preform layers (total thickness 1.89 mm, which is the same as the depth of the features) were pre-formed in this way, with the eighth and final ply stacked on top. The low manufacturing rank is due to the time-consuming and labour-intensive pre-forming operation which would be complex to integrate into high-volume production. Although this method presents similar challenges as in step 2 of the TTR

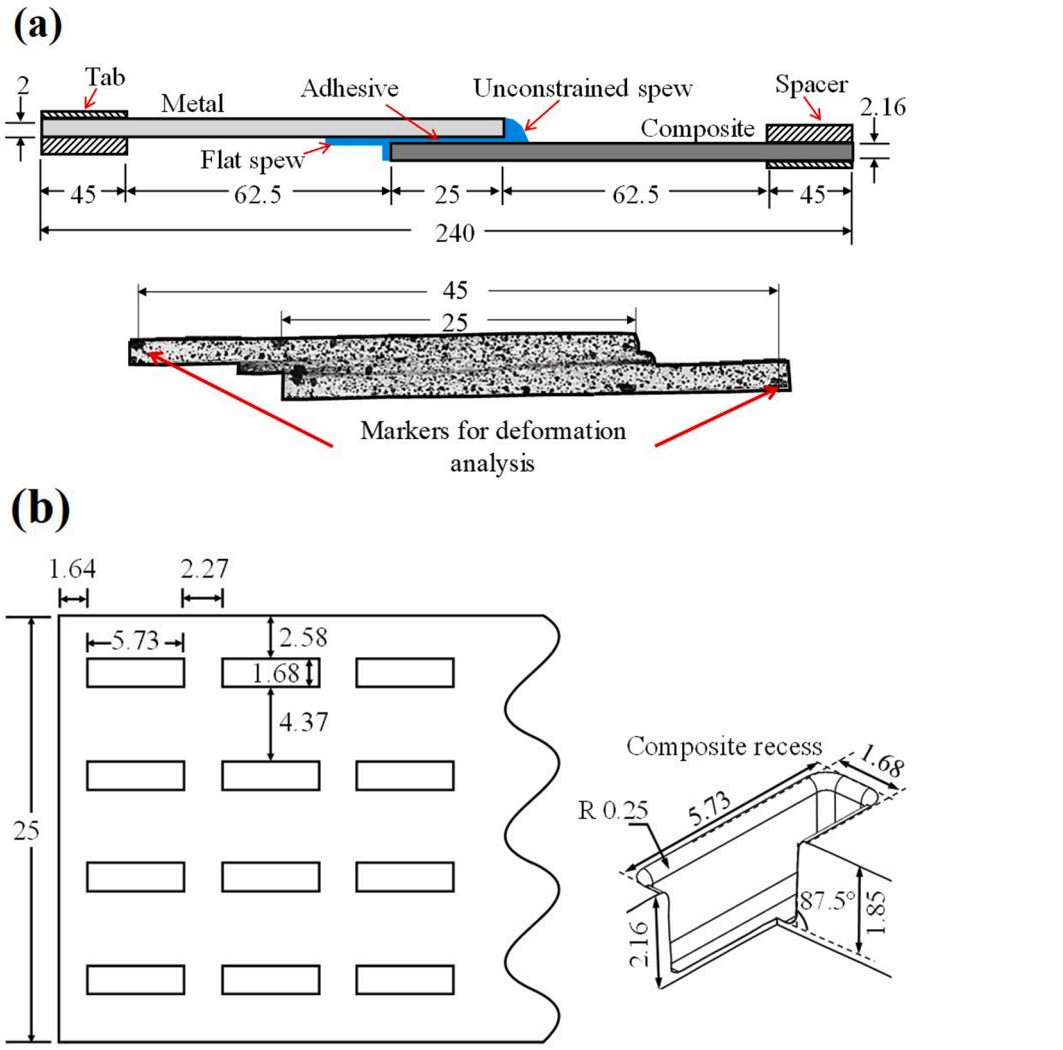

Fig. 2. Single lap joint: (a) joint dimensions and speckled surface for analysis of strain and deformation, (b) geometry of interlocking features in IAJ. All dimensions in mm. (For interpretation of the references to colour in this figure legend, the reader is referred to the web version of this article.)

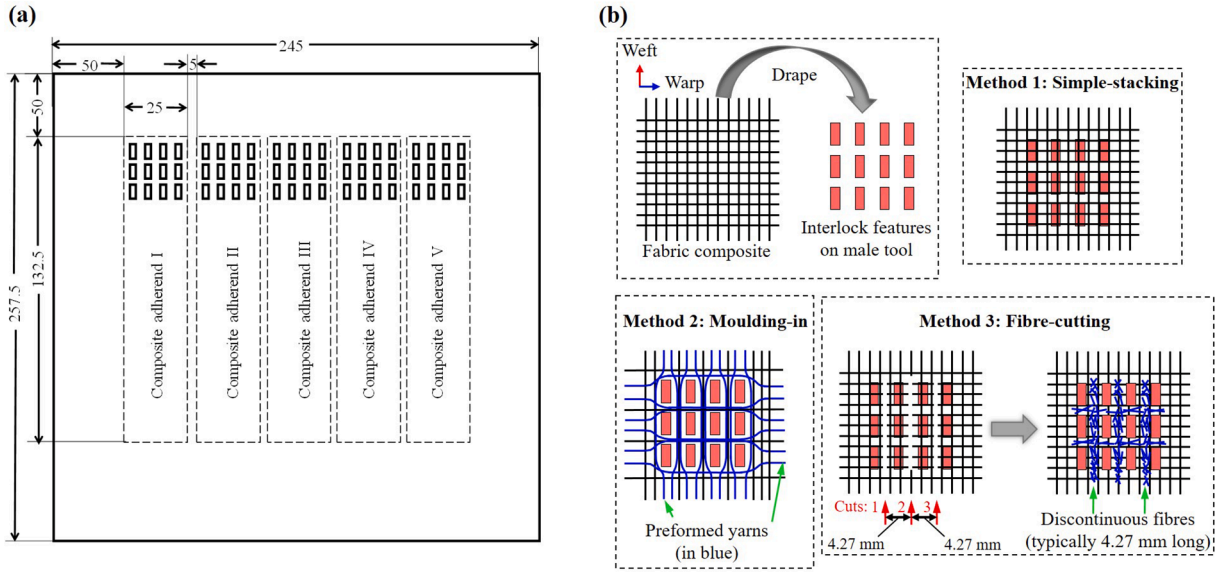

Fig. 3. Composite adherend manufacturing: (a) mould-tool, (b) draping methods. All dimensions in mm. (For interpretation of the references to colour in this figure legend, the reader is referred to the web version of this article.)

joining process described earlier, an additional step to automate the preforming operation can be designed. IAJs offer this potential flexibility due to the use of macro-scale features and secondary bonding, compared to other TTR joints which employ small pins/protrusion and co-curing.

Method M3 – "Fibre-cutting" (Rank 2): In this method, three cuts (cuts 1, 2 and 3 in Fig. 3(b)) are made in the weft direction using a vacuum-assisted CNC ply cutter. The length and position of the cut are precisely controlled to minimise the effect such as fibre-breakage, resin-rich pockets, and fibre-waviness. The cut-length is set to 13 mm, which is 52% of the overlap length. This optimal value was obtained through experimental trials, assessing the conformability of the weave around the interlocking features for different cut-length values. Note that the cut-length value needs to be re-optimised for any change in weave architecture or the interlocking feature geometry. Each cut was centred along the overlap length and positioned at the mid-width of the adjacent rows of interlocking features. This method results in a locally hybridised discontinuous long-fibre/woven-continuous-fibre composite in the region around the features. Discontinuous, long-fibre thermoplastic composites offer high productivity, with good mechanical properties, making them attractive for high volume applications like the automobile industry [31–33], while hybrid long-fibre/woven-continuous fibre composites have been reported to have excellent strength and rigidity [31,32]. The resulting discontinuous warp yarns (typically 4.27 mm long, which is the distance between the cuts) become randomly oriented, while the weft yarns are relatively undamaged. Again, this process was performed on seven plies, with the eighth ply stacked on top. As this method involves a simple added operation that is adaptable to a production environment, it is ranked second in terms of ease of manufacturing. In the literature, TTR reinforcements (in composites) have been reported to lead to a reduction in in-plane mechanical properties due to fibre waviness, resin-rich pockets, and fibre crimp/-breakage. However, for bonded SLJs, since the loads are transferred from the faying surface through the thickness of the composite, a reduction in in-plane properties inside the over-lap region due to the cutting process is not expected to significantly affect joint performance.

Following the above draping processes, the plies and mould-tool were vacuum bagged and consolidated in the autoclave at 240 °C and 600 kPa for 50 min. The temperature and pressure ramp-rates were 3 °C/min and 50 kPa/min, respectively. Although this material system is suitable for high-productivity processes, an autoclave process was employed to reduce manufacturing variability.

2.3. Surface pre-treatment and joint specimen preparation

The pre-treatment process for aluminium adherends followed the alkaline etching process recommended in [34]. For the composite adherends, an optimised alumina grit-blasting procedure described in our previous study [35] was employed. Ultra-pure (99.81%) aluminium oxide (Al_2O_3) blast media (Guyson International Limited, UK) having an angular grit shape, a mean grit size of 220 μm, and measuring nine on the Mohs hardness scale was employed. This process was performed in a heavy-duty blast cabinet (Clarke power products UK) at an air pressure of 172 KPa, through a 4 mm diameter spray nozzle held perpendicular to the bond area at a distance of approximately 300 mm, and moved back and forth along the loading direction, for 20 s. The grit-blasted surfaces were degreased with acetone, ultrasonically rinsed in DIW for five minutes, and dried in the oven at 80 °C for 16 h, before bonding. This optimised process produced a composite surface with plasticised matrix, minimal fibre exposure, minimal release-agent residues, and favourable surface chemistry for adhesive bonding, resulting in the highest lap-shear strength and work-to-failure.

The surface-prepared adherends were bonded in a mould to ensure consistent joint alignment. Bondline thickness was controlled by adding 250 μm glass microbeads. Bonding was performed in an oven at 180 °C for 60 min, following the manufacturer's recommendations [36]. The bondline thickness was found to vary less than ± 10% of the desired value. As illustrated in Fig. 2(a), the adhesive spew was allowed to take an unconstrained "oval" shape at the metal free end, while a flat adhesive spew was enforced by the use of a shim at the composite free end during the bonding process. A trial study of spew shapes on BAJs showed that this configuration yielded the best repeatability and joint performance. Detailed microscopic examinations of untested IAJs, at various sections along the overlap width and length, confirmed a uniform bondline without voids, isolating the aluminium and composite. Thus, minimising the risk of galvanic corrosion in IAJs.

2.4. Mechanical testing

Quasi-static (QS) tests were conducted at 1 mm/min on a tensile test machine (Tinius-Olsen) with a 25 kN load-cell. Dynamic tests at 0.5 m/s and 3 m/s were performed on a Zwick HTM5020 high-speed servo-hydraulic test machine. In the dynamic tests, the load was recorded using a 50 kN piezo-electric load washer (Kistler9051a), at a sampling frequency of 0.95 MHz, with no inbuilt filter employed. As shown in Fig. 2 (a), one side of the specimen was speckled for full-field strain measurements using two-dimensional digital image correlation (2D-DIC) with LAVision Strainmaster software. In addition, joint deformation was obtained from the relative displacement of identifiable black dots (Fig. 2 (a)) separated by 45 mm. For the dynamic tests, a Photron SA1.1 high-speed camera recorded the tests at 100,000 frames per second (fps), with a resolution of 512 × 92 pixels. For QS tests, a LAVision camera at 14 fps was employed. For each composite adherend manufacturing method, three IAJ test repeats were performed at each test speed.

2.5. Optical microscopy

To measure the fibre volume fraction (V_f) and examine microstructural composite damage, optical microscopy was performed using a Zeiss Axioscope at a magnification of 5X, with a resolution of 1.295 μm. The overlap region of the composite adherend was mounted in two-part epoxy with a mixing ratio of four parts of epoxy resin to one part of hardener and cured. Later, using a Buehler Automet™ 300 sample preparation system, the sample was gradually wet-ground to the plane of interest using abrasive paper with varying grit-size (P320 – P1200). Finally, a 0.3 μm alumina suspension solution was used for polishing. Sufficient overlaps between micrographs allowed stitching them to obtain a high-resolution image for the analysis.

3. Results and discussion

3.1. "Apparent" lap shear strength and work to failure

Joint performance is assessed using "apparent" lap shear strength (LSS), and work-to-failure (WF). The LSS is given by ASTM D 5868 [24]:

$$LSS = F_{max}/A_{nom} \tag{1}$$

where F_{max} is the peak force and A_{nom} is the nominal overlap area. The WF or energy absorbed is:

$$WF = \int_0^{\delta_{max}} F(\delta)d\delta \tag{2}$$

where $F(\delta)$ is the force and δ is the deformation of the gauge length.

Fig. 4(a), (b), and (c) present representative force-deformation curves for the BAJs and the IAJs tested at QS, 0.5 m/s, and 3 m/s loading rates, respectively. The manufacturing methods are labelled M1 (simple-stacking), M2 (moulding-in) and M3 (fibre-cutting). As can be seen, the composite manufacturing method had a relatively small (11% or less) effect on F_{max} (particularly at dynamic loading rates) but had a much larger effect on the deformation at failure, δ_{max}. The joint behaviour is strongly influenced by the low yield strength and high ductility of

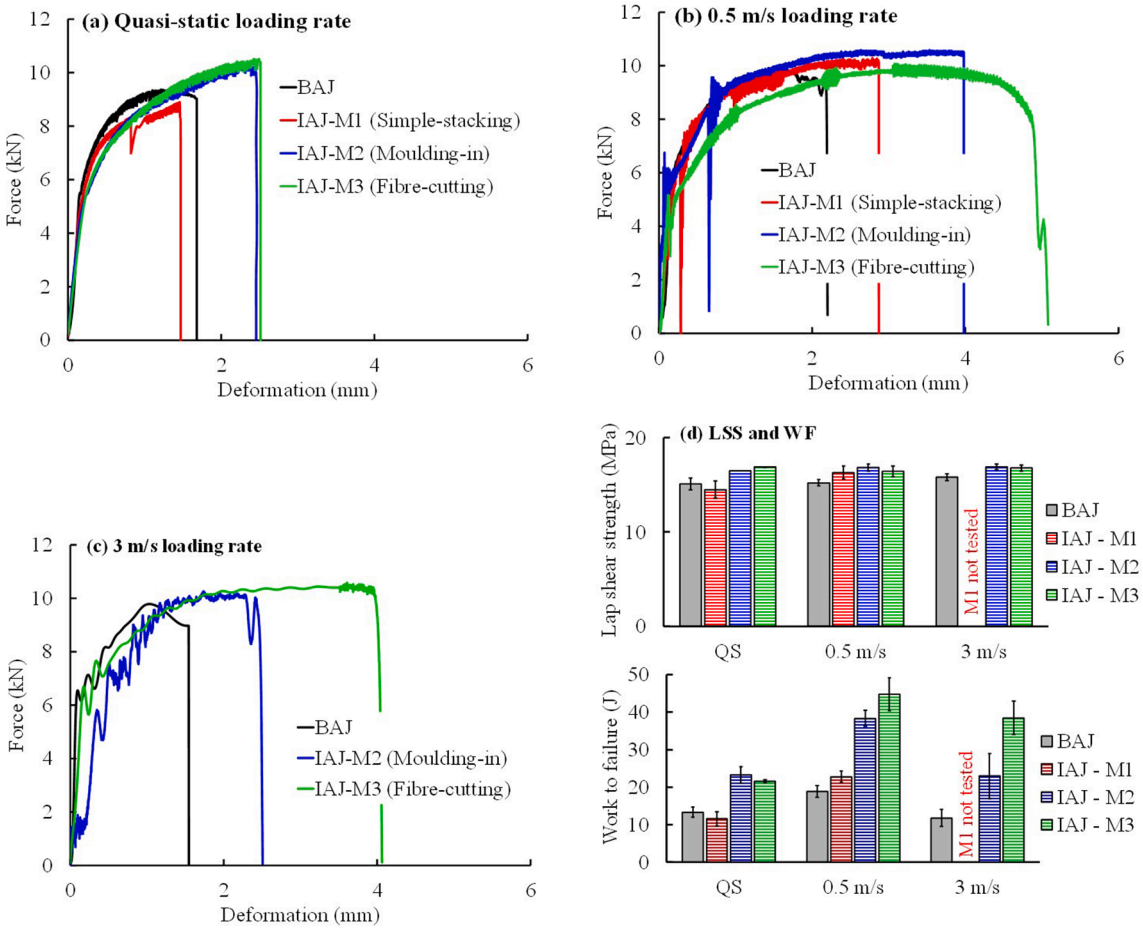

Fig. 4. Representative load versus deformation responses of joints tested at (a) quasi-static, (b) 0.5 m/s, and (c) 3 m/s loading rates, (d) lap shear strength and work to failure for all tests. (For interpretation of the references to colour in this figure legend, the reader is referred to the web version of this article.)

the aluminium. From Table 3, the 5-series alloy used here has a yield stress of 115 MPa, so under pure tensile load the aluminium adherend would yield at a load of 5.75 kN. With the addition of bending stresses due to the single-lap configuration, the inner surface yields somewhat before the joint load reaches this value (evidence to follow). Extensive plastic deformation and strain localisation then occurs before joint failure.

On the other hand, the effect of adherend properties on the mechanical behaviour of bonded joints with similar and dissimilar adherends has been extensively studied in the literature [37–42]. Generally, in joints employing toughened adhesives, the higher the adherend's yield strength, the higher the LSS. This is because the elastically deforming adherend promotes: (a) adhesive global yielding behaviour, where the complete overlap area participates in load transfer, and (b) minimal joint rotation, consequently low adhesive peel stresses. Therefore, in IAJs involving materials with high yield strength, like 6-series or 7-series aluminium, significant increases in F_{max} and LSS is expected, relative to the corresponding BAJs.

Fig. 4(d) presents the average LSS and WF for all tests, with the error bars indicating one standard deviation. The M1 joints did not result in significant improvements in either LSS or WF over BAJs at QS and 0.5 m/s loading rates. This insignificant performance increases for M1 joints will be correlated later with the evidence of poor fibre distribution and extensive composite damage (Section 3.5). Note that for the M1 joints under QS loading, an audible "crack" was heard at a load of about 8 kN, suggesting significant damage in one of the adherends. Similarly to the tests at 0.5 m/s loading rate, relatively small increases in performance is expected for the M1 joints at 3 m/s and hence, they were not tested.

Relative to the BAJs, manufacturing methods M2 and M3 show an approximately 10% higher LSS at all test velocities, while the M1 joints display a 4% lower and 7% higher LSS at QS and 0.5 m/s loading rates respectively. The manufacturing method has a much more significant effect on WF, especially at dynamic loading rates. At the QS rate, relative to the BAJs, the M1 joints exhibit a 5% decrease in WF, while M2 and M3 joints show a 75% and 62% increase respectively. At 0.5 m/s, the M1, M2, and M3 joints display 31%, 120%, and 157% increases respectively relative to BAJs. At 3 m/s, the M2 and M3 joints show 95% and 226% increases respectively relative to BAJs.

Table 4 presents LSS, WF, δ_{max}, failure modes and "mould position" for all the tests. Mould position refers to the position of the composite adherend, from I to V, in the composite manufacturing mould shown in Fig. 3. During autoclaving, fibre re-distribution results in varying levels of lateral constraint for the five specimens in the mould, with the centremost adherend (adherend III) experiencing the largest constraint. Consequently, it was ensured that at least one repeat for each IAJ manufacturing method and test speed had an adherend from position III. As can be seen repeat R4 for the M1 joint tested at 0.5 m/s had an adherend from position III, and displayed a reduced performance (see numbers with an asterisk - LSS = 15.25 MPa, WF = 15.33 J, compared to an average of 16.61 MPa and 22.79 J for the other repeats), indicating the sensitivity of the simple-stacking method to mould position. In contrast, the performance of the M2 and M3 specimens was essentially independent of the adherend location within the mould.

Concerning failure mode, as seen in Table 4, the BAJs always failed in the bondline. The IAJs under QS loading failed in the bondline regardless of the manufacturing method, whereas, at dynamic rates, the

Table 4
Performance metric and failure modes for test repeats.

Loading rate	Metric	BAJ	IAJ – M1 (simple-stacking)					IAJ – M2 (moulding-in)				IAJ – M3 (Fibre-cutting)				
		Mean (SD)	R1	R2	R3	R4	Mean (SD)	R1	R2	R3	Mean (SD)	R1	R2	R3	R4	Mean (SD)
QS	LSS (MPa)	15.1 (±0.61)	14.64	15.76	14.24		14.9 (±0.79)	16.48	16.5	16.48	16.5 (±0.09)	16.89	16.82	16.73		16.8 (±0.08)
	WF (J)	13.2 (±1.19)	13.82	12.84	10.62		12.4 (±1.64)	20.53	23.2	25.91	23.2 (±2.69)	22.01	21.18	21.51		21.6 (±0.42)
	δ_{max} (mm)	1.7 (±0.10)	1.8	1.82	1.47		1.7 (±0.20)	2.46	2.77	2.99	2.7 (±0.27)	2.76	2.51	2.54		2.6 (±0.13)
	Mould position	N/A	V	I	III			IV	V	III		II	III	V		
	Failure mode	BL	BL	BL	BL			BL	BL	BL		BL	BL	BL		
0.5 m/s	LSS (MPa)	15.2 (±0.35)	16.1	16.47	17.22	15.26*	16.6 (±0.55)	16.94	17.2	16.28	16.8 (±0.48)	17.03	16.59	15.67		16.4 (±0.69)
	WF (J)	17.4 (±0.14)	23.1	24.42	20.87	15.33*	22.8 (±1.79)	37.68	41.16	36.08	38.3 (±2.61)	40.3	50.78	43.23		44.7 (±5.41)
	δ_{max} (mm)	2.1 (±0.38)	2.73	2.79	2.41	1.88*	2.7 (±0.20)	3.98	4.3	4.05	4.1 (±0.17)	4.19	5.41	5.08		4.9 (±0.63)
	Mould position	N/A	II	I	II	III		V	III	IV		V	II	II		
	Failure mode	BL	BL	BL	BL	BL		Metal	Metal	Metal		Metal	Metal	Metal		
3 m/s	LSS (MPa)	15.7 (±0.38)						17.03	17.2	16.42	16.9 (±0.40)	17.17	16.42	16.94	16.48	16.8 (±0.36)
	WF (J)	11.8 (±0.38)						17.46	31.31	20.11	23.0 (±7.35)	43.38	34.01	37.93	34.49	37.5 (±4.32)
	δ_{max} (mm)	1.4 (±0.25)		Not tested				2.08	3.44	2.51	2.7 (±0.70)	4.59	4.51	4.06	4.40	4.4 (±0.23)
	Mould position	N/A						III	II	V		II	I	IV	III	
	Failure mode	BL						Comp	Metal	Comp		Metal	BL	BL	BL	

LEGENDS: * - not included for computation of mean and SD; δ_{max} – Joint deformation at failure; BL – Bondline; SD – Standard Deviation; N/A – Not Applicable.

manufacturing method significantly influenced the failure mode. At 0.5 m/s, the M1 joints displayed a bondline failure while the M2 and M3 joints failed in the metal adherend. At 3 m/s, two of the three M2 joints failed in the composite adherend, while three of the four M3 joints failed in the bondline. The joints with the largest WF are the ones in which the metal adherend failed, namely all the M2 and M3 joints at 0.5 m/s loading rate, and repeat R2 of the M2 joints and R1 of the M3 joints at 3 m/s. This indicates that for this combination of materials, plastic deformation of the aluminium adherend is the primary contributor to WF. If the joint holds together long enough for the aluminium to fail, high work to failure is attained. However, it is interesting to note that despite metal adherend failure for all M2 and M3 joints at 0.5 m/s loading rate, the average WF for M3 joints is 17% higher than the M2 joints. The reasons for this difference are discussed when examining the transverse adherend deflections and post-test photographs and micrographs (Section 3.5). In summary:

- The simple-stacking manufacturing method (M1) shows inferior mechanical performance to the moulding-in (M2) and fibre-cutting (M3) methods, and is more sensitive to position in the mould.
- Methods M2 and M3 show similar performance under QS loading but M3 is superior (i.e. has a higher WF) under dynamic loading (particularly at 3 m/s).
- Comparing the WF of the seven IAJs tested at 3 m/s (three M2 and four M3), Table 4 indicates that the most beneficial failure mode for energy absorption is metal adherend failure, followed by bondline failure, followed by composite failure. Failure of the composite adherend is clearly undesirable, but the creation of recessed features makes it a possibility. The manufacturing method for creating these features will be shown later to have a major bearing on whether the composite fails or not.

3.2. Main events in IAJ failure

The mechanical behaviour of IAJs has been studied in detail in our earlier paper [21] and is summarised here. Using DIC analysis it was determined that there are four adhesive "zones" with different types of strain, as shown in Fig. 5(a). At the overlap ends, zone A, the adhesive experiences a combination of peel and shear strains. In the region sloped at $+45^{\circ}$, zone B, the adhesive experiences predominantly tensile strains as the interlocked surfaces are moving apart. Conversely, in the region sloped at -45°, zone D, the adhesive is in compression. Finally, the adhesive in the horizontal region at the top of the feature, zone C, is loaded in shear.

Fig. 5(b) illustrates the sequence of damage and failure events in the IAJs observed in [21] via extensive DIC analysis, and also observed with the current experiments. Due to the eccentric load path, the adherends stretch and bend (so-called "secondary bending"), which leads to rotation of the bonded region. The first non-linearity in the load-deflection curve (event 1) is when the aluminium adherend yields at its inner surface where the combined tensile/bending stresses are highest. This increases the joint rotation and causes high peel stresses in the adhesive at the composite free end. Consequently, the primary adhesive crack (event 2) *always* initiates at the composite free end. Upon further loading, the primary crack propagates into the overlap, but stops at zone D of the first interlocking feature, due to the compressive adhesive stresses at that location. Due to this temporary halt in primary crack propagation, a secondary crack (event 3) sometimes initiates at the aluminium free end, which rapidly propagates into the overlap region, through zones A, B and C where the adhesive is in tension and/or shear, before potentially stopping at the first zone D it encounters. The presence of zones of compressive strain in the adhesive is thus a useful feature of the IAJs in arresting the crack propagation.

Ultimate failure (event 4) tends to occur differently under QS and dynamic loading. In the QS tests, as the load increases the joint continues to stretch and rotate, and the surfaces in zone D rotate into closer

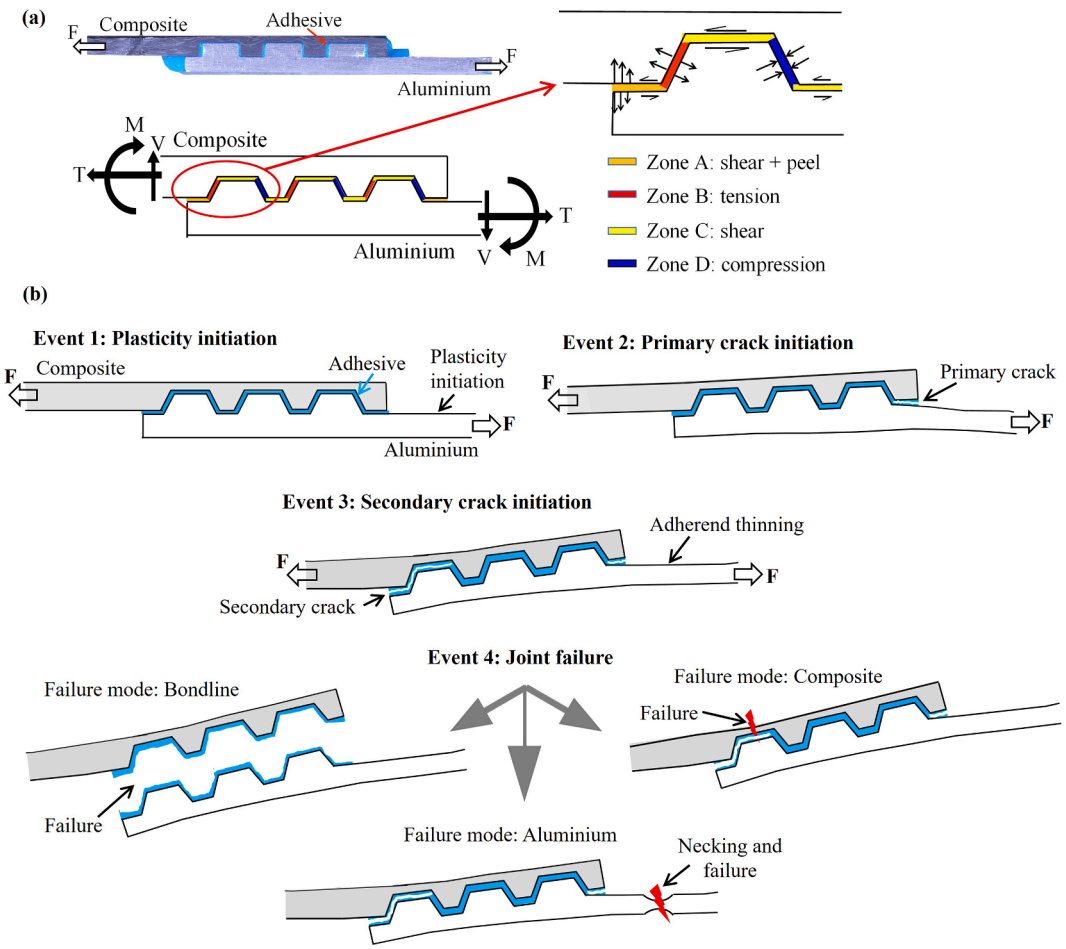

Fig. 5. Schematics of interlocking joint behaviour observed in [21], (a) strain-state from DIC results and (b) damage initiation and propagation, and final failure modes.

alignment with the loading direction, which changes the strain type from compression to shear. This allows the cracks to propagate through this zone, resulting in catastrophic bondline failure. In the dynamic tests, crack propagation is sufficiently resisted by the interlocking features for joint failure to occur either progressively in the aluminium due to strain localisation and necking, or catastrophically in the composite, near the first row of interlocking features at the metal free end. As seen above if composite adherend or bondline failure occurs the energy available from plastic deformation of the metal adherend is not fully availed of and WF is reduced accordingly.

3.3. *Thickness, fibre-volume fraction (V_f) and fibre distribution analysis of manufactured samples*

To assess the quality of the recessed features, thickness and fibre volume fraction (V_f) measurements were made on untested composite adherends. The fibre volume fraction and distribution turn out to be key factors in joint behaviour. As illustrated in Fig. 6(a), section micrographs were taken at transverse cross-sections A-A and A′-A′, and longitudinal sections B-B and B'-B', all of which pass through the interlocking features. Measurements of thickness were made for two specimens manufactured by each method. The overall values for H, the thickness of the non-recessed regions, shown in Fig. 6(b), are each an average 92 measurements, and the values for h, the thickness of the recessed regions, are each an average of 80 measurements. For the fibre volume fraction measurements, the transverse sections, A-A and A′-A′ were broken into Region I (non-recessed areas), and Region II (recessed areas), see Fig. 6 (a). Because of significant variation in V_f in Region I, a further measurement was made of the protruding portion of that region (Region Ia). Similarly, the longitudinal sections B-B and B′-B′ were broken into Region III and IV. Two specimens manufactured by each of the three methods were used in the V_f calculations.

The thickness measurements (Fig. 6(b)) show that all thicknesses were above their nominal value. This is true especially of the recessed regions. Manufacturing method M1 shows the largest deviation from the nominal values, while the average thicknesses for the M2 and M3 methods are similar.

Fig. 6(c) shows the transverse (A-A and A′-A′) section volume fraction measurements. The fibre volume fraction in the recessed regions (region II) is satisfactory, with all methods giving $V_f = 48\%$ or more, which is close to the nominal value of 52%. However, Method M1 (simple-stacking) has a serious problem in the non-recessed regions (region I) with $V_f = 31\%$. Furthermore, the problem is seen to be especially severe in the protruding portion (region Ia) where V_f is just 10%. The micrograph in Fig. 6(e) confirms the extremely low fibre content in the protruding portions across the entire width of the M1 specimen. The effect of this will be to lower the bending stiffness and strength at the feature locations. This will be seen later to be crucial at the row of features nearest the aluminium free end, where the composite experiences high bending stress.

Method M2 (moulding-in) shows some improvement with V_f being equal to 33% and 17% in regions I and Ia respectively. The improvement in the protruding sections (Ia) is clearly visible in the corresponding micrograph in Fig. 6(g). Method M3 (cut-fibre method) shows by far the best results for the transverse sections, with V_f being equal to 42% and 43% in regions I and Ia respectively. The micrograph in Fig. 6(i)

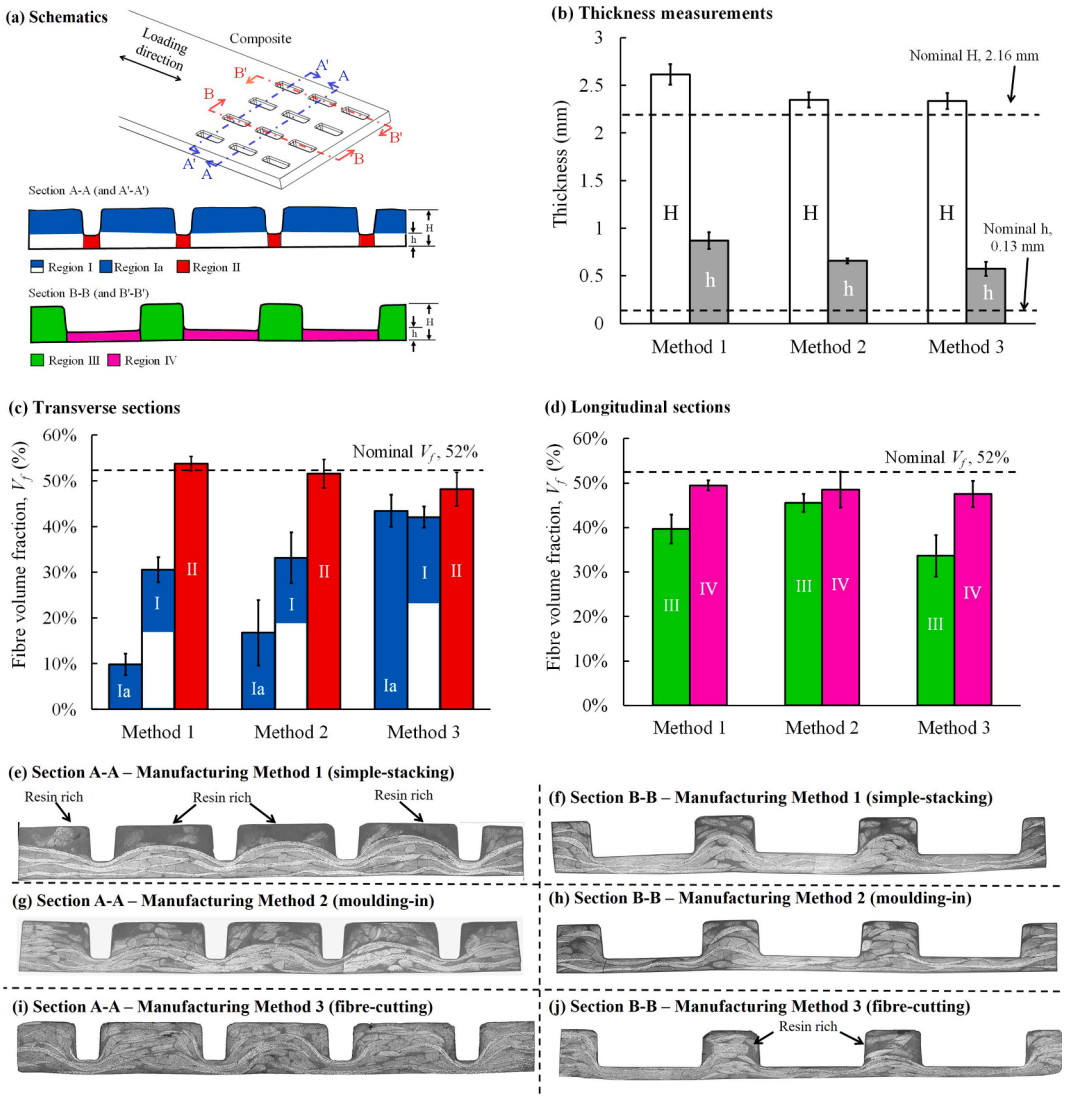

Fig. 6. Thickness and fibre-volume fraction (Vf) analysis, (a) schematic illustrating different sections and regions, (b) thickness measurements, (c) Vf for transverse sections, (d) Vf for longitudinal sections, (e) – (j) micrographs of section A-A and B-B, for the three manufacturing methods. (For interpretation of the references to colour in this figure legend, the reader is referred to the web version of this article.)

confirms the very good fibre content in the protruding sections (region 1a) across the full width of the adherend. This will provide much better flexural properties than for methods M1 or M2. Recall from Table 4 that there were no cases of composite adherend failure in M3 joints at any of the test speeds.

The longitudinal sections (Fig. 6(d)) again show good fibre volume fraction (47–49%) in the recessed regions (region IV). The results for the non-recessed regions (region III) are not as good but the problems are not nearly as severe as for the transverse sections. The micrographs in Fig. 6(f), (h) and (j) confirm the moderate nature of the issues. Unlike for the transverse sections, M3 displays the lowest fibre volume fraction in region III (34%) and some resin-rich regions can be seen in the protruding areas in Fig. 6(j). On first consideration this would appear to be a disadvantage for method M3, but in fact it proves to be a serendipitous advantage. The protruding regions along the longitudinal sections experience compressive loads from the metal features. As will be shown later (Section 3.5), the low V_f facilitates the aluminium interlocking features locally indenting the resin-rich pockets at the region III, improving the interface between the composite and adhesive.

The variability in thickness and volume fraction is due to the weave not being flexible enough to accommodate macro-scale features. The fibre-cutting method (M3) significantly improves the flexibility of the fabric composite, resulting in the lowest thickness, and the most uniform fibre volume fraction. Similar issues with thickness and fibre volume fraction have been reported with Z-pinning [43,44], especially with a high density of pins. On the other hand, defects like voids, porosity, and matrix cracking, typically seen in hybrid bonded/pinned joints, were not observed in the current IAJ composite adherends.

3.4. Secondary bending and transverse deflections

In the absence of secondary bending the applied tensile load would result in shear stresses in the adhesive and direct stresses in the adherends. However, secondary bending introduces bending stresses in the adherends and peel stresses in the adhesive, which critically affects joint performance. In the joints studied here, secondary bending has a strong influence, as large joint rotations occur due to the plastically deforming aluminium. To analyse these secondary bending effects, measurements were made of transverse adherend deflections. The method is illustrated in this section for quasi-static loading of baseline adhesive joints (BAJs). The results for IAJs at all loading rates are shown in the next section.

The deformed shape (exaggerated for clarity) is illustrated in Fig. 7 (a). Secondary bending results in transverse deflections, w_c and w_m which are functions of distance along the adherend lengths, x_c and x_m.

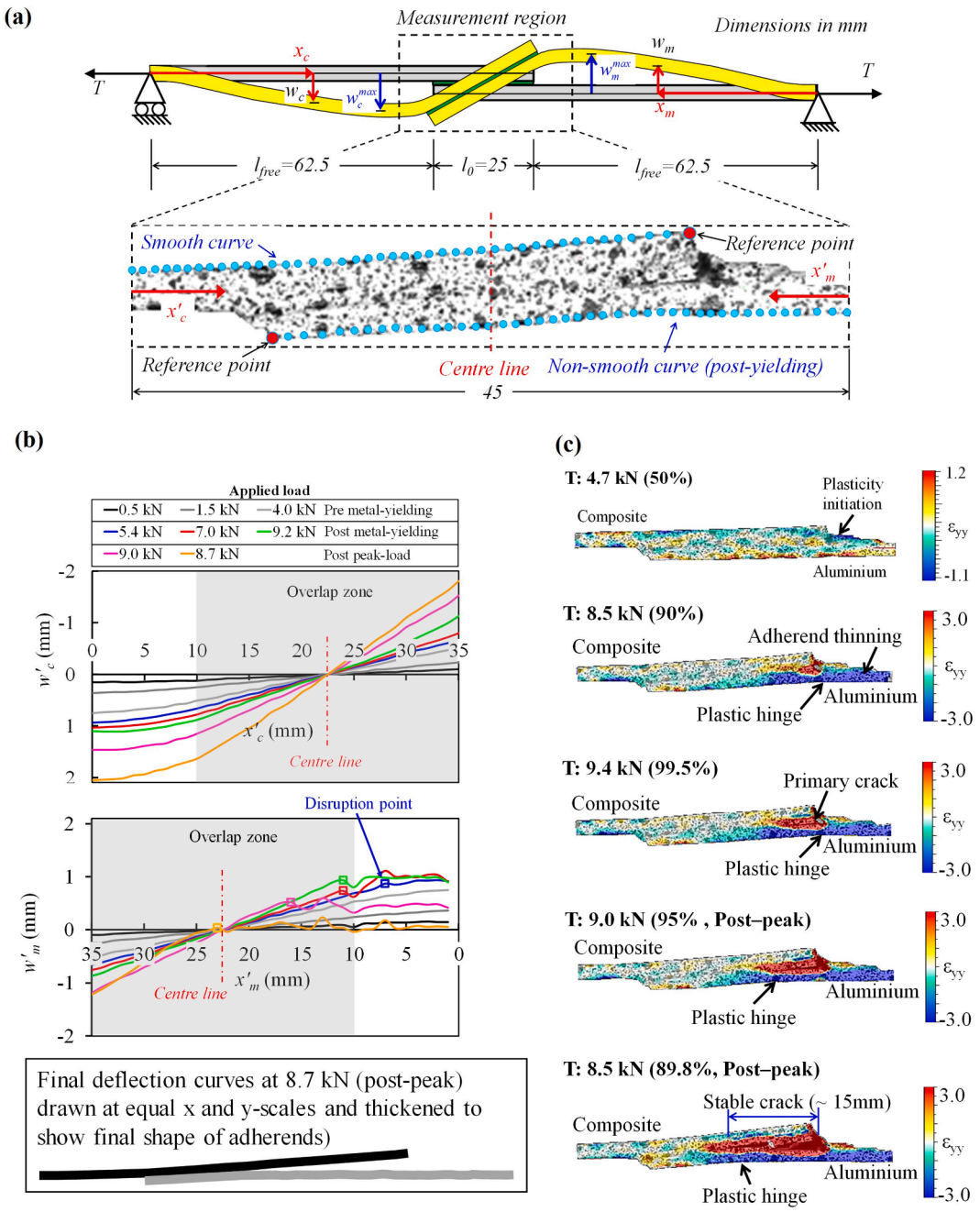

Fig. 7. Secondary bending in baseline adhesive joint (BAJ) under quasi-static loading, (a) Joint deformation schematic and measurement method, (b) composite (w_c), and aluminium (w_m) transverse deflections at selected load levels (square symbols indicate first occurrence of negative slope or "disruption point"), (c) peel strain contours from DIC analysis at selected load levels. (For interpretation of the references to colour in this figure legend, the reader is referred to the web version of this article.)

While the adherends remain elastic, the maximum deflection generally occurs at a position outside the overlap region, as illustrated. The deflections of points spaced 1 mm apart along the outer surface of each adherend were measured in a 45 mm wide zone, as shown in Fig. 7(a), using DIC analysis. The measured deflections are labelled w'_c and w'_m in Fig. 7(b) because, they were measured using the free-end points (red dots in (a)) as reference points and an arbitrary assumption of zero deflection at the joint centre line. This arbitrary choice of datum was made because the clamped ends of the joint were not in the field of view. Since the main interest here is in identifying the general shape of the deflection curve rather than absolute values relative to the joint ends, this approach is adequate.

In Fig. 7(b), the BAJ deflections are plotted for selected load levels as a function of distance from the end of the measurement region, i.e. x'_c and x'_m, where $x'_c = x_c - 52.5$ and $x'_m = x_m - 52.5$. The apparently odd choice of axis directions (e.g. increasing values of w_c from top to bottom in the composite adherend graph, and increasing values of x'_m from right to left in the metal adherend graph) is to enable the shape of the curves to be directly compared with the picture in Fig. 7(a). Note that the scale of the x and y axes is vastly different. The actual final shape drawn to scale is shown at the bottom of Fig. 7(b).

The first three load levels are below the load at which the metal adherend yields (black/grey curves). At these loads the curves are smooth and the deflection of the composite and metal adherends is similar due to their reasonably similar stiffness (the metal has a higher Young's modulus but is slightly thinner). For the first three load levels

the maximum deflections occur slightly outside the measurement region, as was shown schematically in Fig. 7(a).

The next three load levels (blue, red and green curves) span the range between when the metal yields and when the peak joint load occurs. The curves for the composite remain smooth, but the smoothness is disrupted for the metal adherend. This can be seen to some extent in Fig. 7(a) and much more clearly in Fig. 7(b). The "disruption point" (identified by the first sharp negative slope) is initially outside the overlap region, but as the load increases, it moves towards, and eventually into, the overlap zone. The final two load levels (pink and orange curves) show the situation after the peak joint load has occurred. Just prior to final joint failure (orange curve), the disruption point has moved beyond the centre line of the joint, and the transverse deflection of the metal adherend has reduced to almost zero at the right of the disruption point, indicating the shape of the metal adherend is almost bilinear. In contrast, the curves for the composite adherend remain smooth all the way to joint failure. The final shape of the adherends indicates the existence of a long primary crack in the adhesive.

Fig. 7(c) presents strain contours in the y-direction (which in the adhesive are peel strains) from DIC analysis. Yielding in addition to joint rotation results in the formation of a plastic hinge in the metal adherend at a similar load level to the one that showed a disruption in the transverse deflection curve. The primary adhesive crack then initiates and propagates into the overlap region, and the position of the plastic hinge follows the crack-tip. The position of the disruption point in the deflection data was found to correlate very well with the position of the

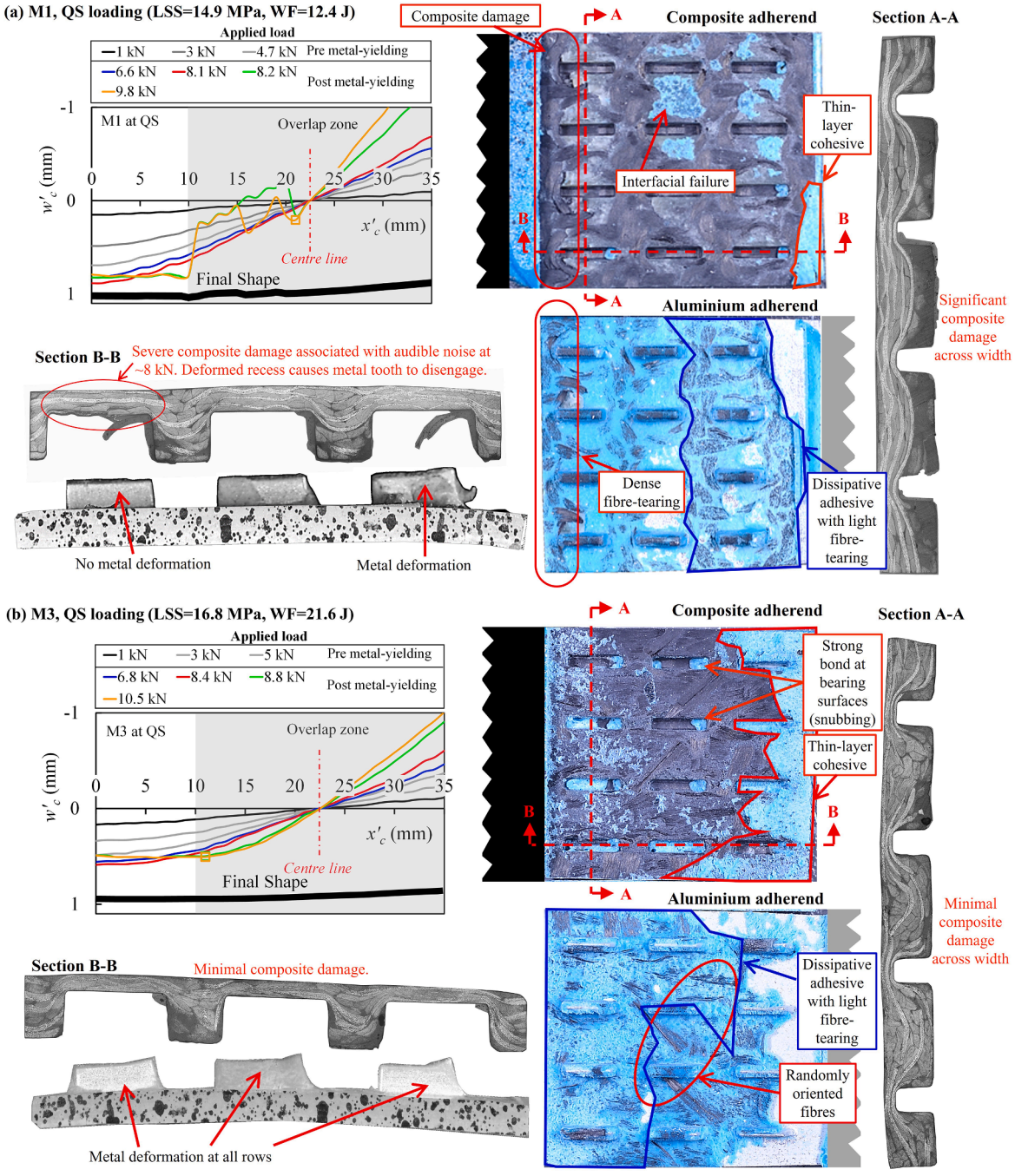

Fig. 8. Composite (w_c) transverse deflection curves at selected load levels, and post-test photographs and micrographs for IAJ's under quasi-static loading. (For interpretation of the references to colour in this figure legend, the reader is referred to the web version of this article.)

plastic hinge in the DIC images, at all load levels. The final DIC image in Fig. 7(c) can be seen to match the final shape of the adherends obtained from the transverse deflection data extremely well. The transverse deflection method comes into its own in the dynamic tests for which the DIC strain images are much harder to interpret because of the relatively low camera resolution. It proves to be highly sensitive for picking up major events like primary or secondary crack formation or composite damage.

3.5. Fractography and deflection analysis of the IAJs

In this section, selected cases are chosen for detailed analysis via transverse deflections, and post-test photographs and micrographs. Fig. 8(a) shows an M1 joint tested under QS loading. Only the composite adherend deflections are shown, since the aluminium deflections follow a similar pattern to the BAJ in Fig. 7. Unlike the BAJ, the smoothness of the composite deflection curves is lost at 8.2 kN (green curve), as identified by comparing the deflection curves at 8.1 kN (red curve) and 8.2 kN (green curve). The disruption is severe, and even in the final shape drawn to scale, the non-smooth shape between the edge of the overlap and 11 mm into the overlap is clear. The transverse section A-A micrograph shows damage in the composite, including matrix cracking and delamination across the width of the first row of features, particularly in the protruding portions which are starved of fibres when the M1 manufacturing method is used. The low bending stiffness at the feature locations leads to large deflections, and the longitudinal section B-B micrograph reveals severe composite damage in the recessed portion of the first feature (from the metal free end). This is the cause of the audible "crack" in the tests at about 8 kN applied load as well as the disruption of smoothness of the composite deflection curves. Further, this damage leads to widening of the recess, and disengagement of the first row of metal features, as is evident from the lack of any deformation in the metal at that row. It also leads to rotation of the overlap region, which allows the adherends to pull apart at a relatively low load. The extensive composite damage near the first row of features is also visible in the composite adherend photograph. Concerning adhesive failure modes, as defined in ASTM D5573-99 standard [45], the composite adherend shows small areas of "thin layer cohesive" and "interfacial" failure, while the aluminium adherend reveals a larger area of "dissipative adhesive failure with light fibre tearing", and an area of "dense fibre tearing" in the region of the secondary crack (metal free end).

Fig. 8(b) shows the same set of images for an M3 joint tested under QS loading. The M3 adherend clearly has a higher bending stiffness than the M1 adherend, as evidenced by the smaller deflection at similar load levels (e.g compare the blue curves in Fig. 8(a) and (b)). This is because of the much higher fibre volume fraction across the width of the features. The smoothness of the deflection curves is unchanged until the last load level (10.5 kN), however a change in shape is observed (8.8 kN). The change in shape is not severe, as can be seen by viewing the deformed shape drawn to scale. In fact, this time the deflection measurements are picking up the initiation of the secondary crack rather than the occurrence of composite damage, as was confirmed by comparison with DIC strain images (not shown). The change in shape is a result of secondary crack initiation, which exposes the recessed region with a reduced area moment of inertia, subjecting the region to high bending stresses. The section micrographs show minimal evidence of composite damage, and the features remain interlocked to high enough loads to deform all rows of the metal features, increasing the WF. Concerning adhesive failure modes, compared to the M1 joint, the M3 joint shows increased areas of thin-layer cohesive and light fibre-tearing failure. In [35], these failure modes have been shown to absorb significant amounts of energy, which adds to the WF for the M3 joints. It is noticeable for the M3 joint that the strands of carbon fibre attached to the aluminium surface are randomly oriented, which is due to the fibre-cutting manufacturing method. Interestingly some of the adhesive remains attached to the composite at locations where the composite features are under bearing load from the metal features. This strong bond eventually leads to "snubbing" in M3 joints at dynamic loading rates, where the composite features are continuously subjected to high bearing loads from the metal features, until the final joint failure.

Fig. 9(a) and (b) show M2 and M3 joints tested at 0.5 m/s. These joints had the highest WF of all test cases (38.3 J for M2 and 44.7 J for M3). The transverse deflection curves for the composite adherend reveal a key reason for this. The curves for both M2 and M3 joints remain smooth with no change in shape, all the way to joint failure (the "ripples" in the curves are most likely due to vibrations at this dynamic loading rate). This reflects the fact that there was no major composite damage nor any secondary crack for these joints. As shown in our previous work [21], the occurrence of a secondary crack immediately leads to a sharp increase in joint rotation. This puts the overlap region of the composite adherend under increased bending stresses making it susceptible to failure. The non-occurrence of the secondary crack shields the composite adherend against experiencing such high bending stresses, and is a key reason why the M2 and M3 joints tested at 0.5 m/s gave the highest WF.

Both M2 and M3 joints ultimately failed in the aluminium adherend due to strain localisation and necking. As can be seen in Fig. 9, for the M3 joints, the necking and failure occurred within the 45 mm region used for measurement of joint displacement by optical extensometry, thus contributing to the calculation for WF. On the other hand for M2 joints, the necking and failure occurred partly outside the measurement region, meaning it did not contribute fully to the calculation of WF. Thus, the difference between the M2 and M3 WF (6.4 J) would likely be less if a longer measurement region had been used. The M2, 0.5 m/s case is the only one where any significant energy-absorbing processes occurred outside the measurement region.

Longitudinal section B-B shows some notable differences between the M2 and M3 joints. Unlike the M2 joint (Fig. 9(a)), the M3 joint (Fig. 9 (b)) shows uneven thickness of the adhesive, i.e., the adhesive has elongated in the zone B tensile region and contracted in the zone D compressive region. This is as a result of aluminium interlocking features locally indenting the resin-rich pockets at the compressive load-bearing regions of the recessed composite features, a process known as "snubbing " in Z-pinning [46]. Recall that the M3 method results in a somewhat low fibre volume fraction (34%) in the non-recessed regions along the longitudinal sections (see region III in Fig. 6). After the primary crack initiates, due to the load redistribution between mechanical interlock and the adhesive layer, the bearing-loaded region of the recessed features is more actively engaged in the load transfer. As the bearing load increases, the aluminium interlocking features are able to penetrate into the composite at locally resin-rich regions. It is also assisted by the fact that at dynamic strain rates, for example at 3200/s, the compressive yield stress of the adhesive [47] is twice that of the thermoplastic resin [48] used in the current study. Finally, bondline failure and deformation in the aluminium interlocking feature are more extensive in the M2 joint (see zoomed micrographs), while as a result of snubbing both are low in M3 joints. In addition, the average primary crack length was 4.75 mm compared to 8.25 mm for M2 joints. References [43,44] report snubbing as a vital strengthening and toughening mechanism in joints with substantial mode-mixity, like SLJs. References [44,49–51] report snubbing to significantly increase the friction between z-pins and the composite, enhancing the resistance against shear-induced pull-out. It is likely that snubbing is a significant contributor to the excellent work-to-failure and reduced damage propagation in the M3 joints.

Fig. 10(a) and (c) present the M2 and M3 joints tested under 3 m/s loading rate. Unlike the other test speeds there is a large difference in WF for these manufacturing methods (23 J for M2, 37.5 J for M3). For the M2 joint, Fig. 10(a), the composite adherend transverse deflection curves remain smooth right up to the peak load (10 kN). The secondary crack then forms, and the last curve indicates a hinge-point (change in slope) in the composite at $x'_c \cong 13$ mm, i.e. at the first row of features.

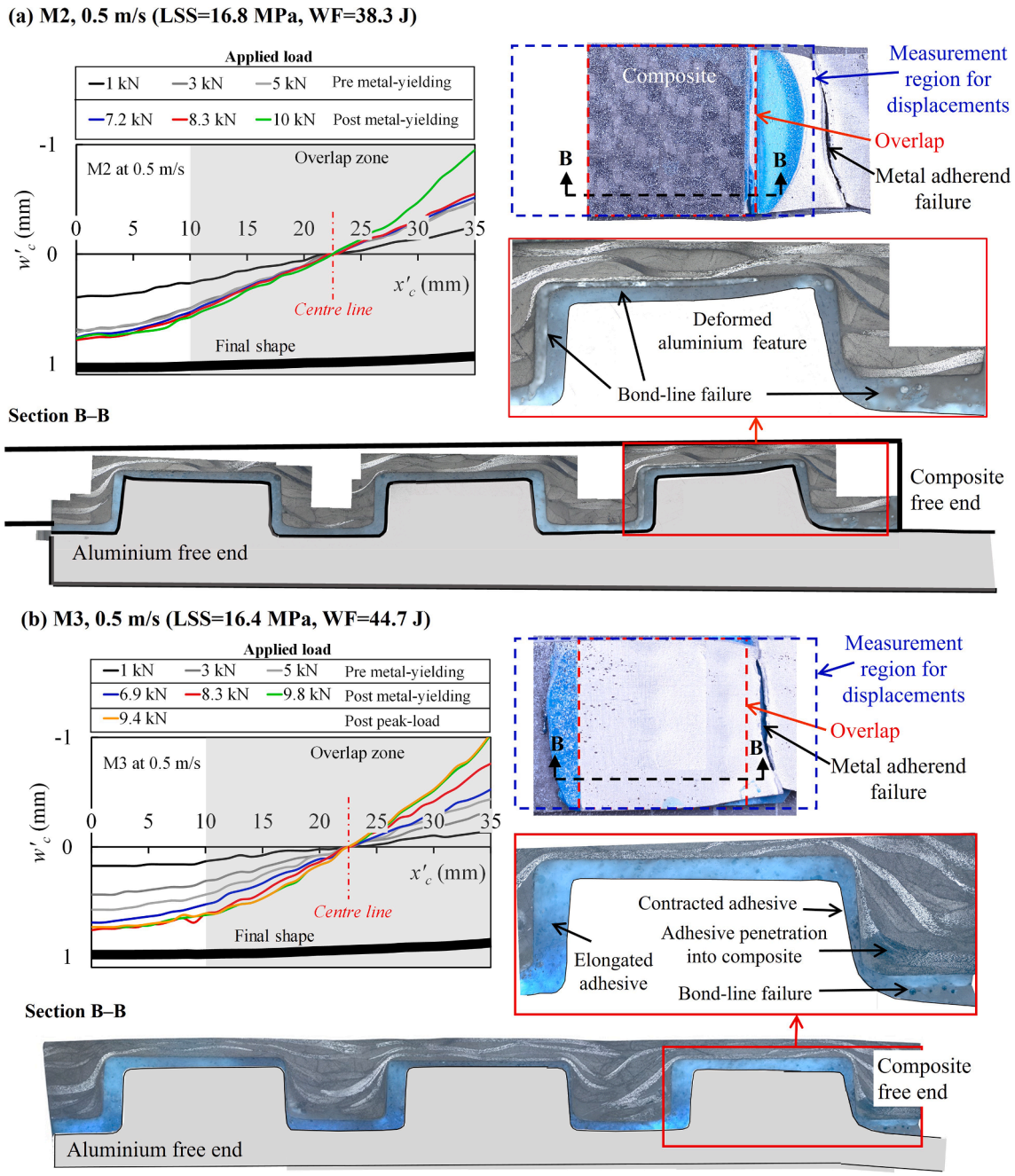

Fig. 9. Composite (w_c) transverse deflection curves at selected load levels, and post-test photographs and micrographs for IAJ's under 0.5 m/s loading. (For interpretation of the references to colour in this figure legend, the reader is referred to the web version of this article.)

Frames from the test videos (top-right) show that almost immediately after the secondary crack appeared, the composite failed completely at this first row of features, ending the test, even though the bend in the composite is relatively mild, as can be seen from the final shape drawn to scale. The photograph (bottom-right) shows the two halves of the failed composite. Recall from Fig. 6 that with the M2 method, V_f in the non-recessed regions of the transverse sections (region I) is 33%, while in the protruding portion of these regions, it is just 17%. This leads to low tensile and flexural strength at the feature locations, making the composite susceptible to tensile/bending failure at the first row of features where the bending moment is highest.

An obvious question is why composite adherend failure did not happen for M2 joints tested at QS and 0.5 m/s loading rates. Fig. 10(b) shows the transverse deflection curves for the M2 joints under QS loading. For QS loading, the secondary crack occurs at a lower load (~8.6 kN) than it does at 3 m/s (10 kN), at which the bending moment is not as high. Consequently the "hinge" (change of slope) does not form. The composite continues to bend as the load gradually increases, and the maximum deflection remains at the edge of the overlap rather than at the first row of features. Because the adhesive is highly strain-rate dependent [52], at quasi-static loading rates it fails before the composite hinge has a chance to form. The reason composite failure did not occur at 0.5 m/s, as mentioned above, is because the secondary crack does not form at 0.5 m/s. This protects the composite from the severe bending moments that occur when the secondary crack forms.

Fig. 10(c) shows that for the M3 joint at 3 m/s, the secondary crack occurs at ~8.1 kN. A hinge forms in the composite adherend, which is then subjected to some extreme bending, as the load increases. Even the

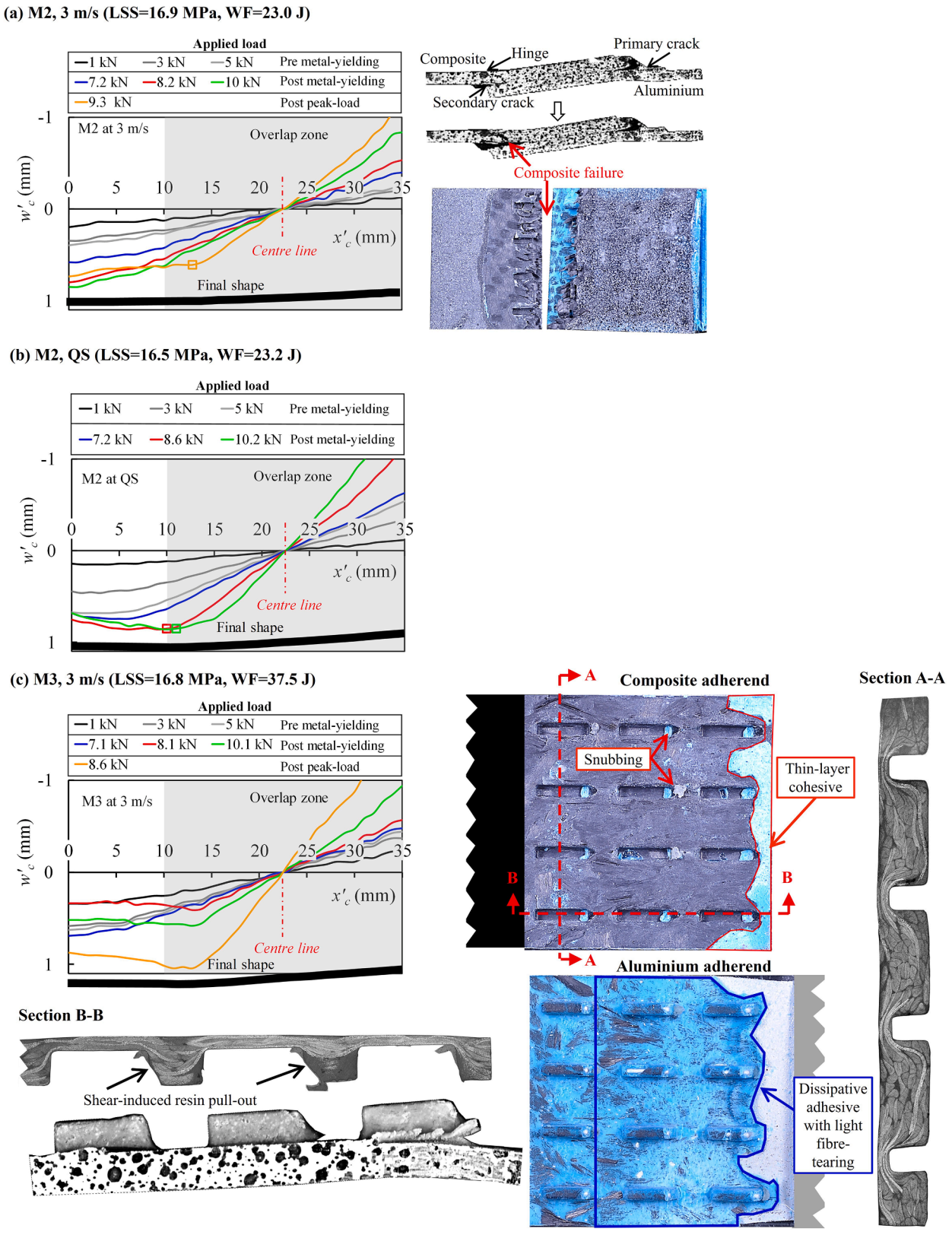

Fig. 10. Fractography and deflection analysis for, (a) M2 joint under 3 m/s loading, top-right: frames from the test video showing composite failure and bottom-right: two-halves of a failed composite, (b) gradually increasing transverse deflections for M2 joint under quasi-static loading, (c) M3 joint under 3 m/s loading. (For interpretation of the references to colour in this figure legend, the reader is referred to the web version of this article.)

final shape shown to scale reveals the level of bending is far more severe than that which led to failure of the M2 composite adherend. However, because of the much higher V_f in regions I and Ia (42% and 43% respectively) the composite is able to sustain this level of bending moment without failing in combined tension/bearing. Instead the failure surfaces of the M3 joint show an eventual "bearing" failure mode in the composite adherend due to the snubbing effect. In the micrographs, section A-A does not show any damage, while the section B-B shows sheared-off resin-rich regions at the edges of the composite features. This progressive shearing-off process is likely to absorb considerable energy and contributes to the high WF for M3 joints. Finally, the side image of the metal adherend shows minimal deformation of the metal protuberances due to snubbing effect.

4. Conclusions

This study aimed to develop a simple, controlled process to manufacture composite adherends with recessed macro-scale interlocking features, for use in hybrid interlocked metal-composite joints. The three manufacturing methods investigated, ranked in terms of ease of manufacture are (1) simple-stacking (M1), (2) fibre-cutting (M3), and (3) moulding-in (M2). Following experimental testing, the following conclusions can be drawn:

1. The ranking in terms of performance is: (1) fibre-cutting (M3), (2) moulding-in (M2), and (3) simple-stacking (M1). The M3 method is the only one to provide excellent performance at all loading rates.
2. The M3 joints recorded 62%, 157%, and 226% higher WF than the corresponding baseline adhesive joints (BAJs), at QS, 0.5 m/s, and 3 m/s loading rates, respectively. The effect on LSS was less significant with both M2 and M3 joints demonstrating approximately 10% higher LSS than BAJs at all loading rates.
3. The primary reasons for the success of the M3 method are:

a) fibre volume fraction of 48% across the overlap width particularly between the recesses was found adequate, leading to good flexural properties capable of resisting the high secondary bending moments which occur in single-lap joints between the materials used here.
b) Somewhat reduced fibre volume fraction along the overlap length in the areas between recesses. This allows the adhesive to penetrate into resin-rich pockets at the bearing surfaces of the features, improving interlocking, a process known as snubbing.

4. The results emphasize the flexural properties of the composite at the recessed features as an important design as well as manufacturing consideration for the TTR composite – aluminium joints susceptible to large rotations. Also, the transverse deflection measurements is a simple yet effective analysis that can provide significant insights into the deformation mechanisms in joints, especially at dynamic loading rates, for which the DIC strain images are generally difficult to interpret because of the relatively low camera resolution.
5. Delaying the occurrence of the secondary crack can be beneficial when the composite has poor properties. At 0.5 m/s the secondary crack did not occur and the weak M2 adherends were protected from the high bending moments that arise when the secondary crack appears.

Overall, the fibre-cutting (M3) method is a simple, controlled process that offers a practical solution for integration into emerging, high-productivity processes like stamp forming or compression moulding, desirable for the automotive industry. Given the high WF achieved with the M3 method, this hybrid joining technology could be a key enabler for lightweight, crashworthy, multi-material automotive structures. However, further experimental work is still required to obtain a detailed understanding of this technique for, the different combinations of adherend materials, composite fabric architecture, and various loading scenarios like damage tolerance, environmental durability, fatigue etc.

CRediT authorship contribution statement

Karthik Ramaswamy: Conceptualization, Methodology, Investigation, Data curation, Formal analysis, Validation, Writing - original draft, Visualization. **Ronan M. O'Higgins:** Conceptualization, Methodology, Visualization, Supervision, Project administration, Resources, Writing - review & editing, Project administration, Resources, Funding acquisition. **John Lyons:** Methodology, Investigation, Visualization, Writing - review & editing. **Michael A. McCarthy:** Conceptualization, Methodology, Visualization, Supervision, Project administration, Resources, Writing - review & editing. **Conor T. McCarthy:** Supervision, Project administration, Resources, Funding acquisition.

Declaration of Competing Interest

The authors declare that they have no known competing financial interests or personal relationships that could have appeared to influence the work reported in this paper.

Acknowledgements

This work was supported by EU Horizon 2020 Marie Skłodowska-Curie Actions Innovative Training Network- ICONIC [grant agreement number: 721256] and financial support of Science Foundation Ireland (SFI) under Grant Number SFI 16/RC/3918, co-funded by the European Regional Development Fund. The authors thank Adrian McEvoy, Brian Nestor and Joseph Leen for their help with experimental facilities, and Antala Limited, UK and Dow Automotive, Germany, for providing the structural adhesive for this research work.

References

[1] European Commission. Roadmap to a Single European Transport Area–Towards a competitive and resource efficient transport system; 2011. 10.2832/30955.
[2] ERTRAC Working Group. Safe Road Transport Roadmap - Towards Vision Zero - Roads without Victims. Brussels, Belgium: European Road Transport Research Advisory Council; 2019.
[3] Delogu M, Zanchi L, Dattilo CA, Pierini M. Innovative composites and hybrid materials for electric vehicles lightweight design in a sustainability perspective. Mater Today Commun 2017. https://doi.org/10.1016/j.mtcomm.2017.09.012.
[4] Bein T, Mayer D, Hagebeuker L, Bachinger A, Bassan D, Pluymers B, et al. Enhanced lightweight design - first results of the FP7 Project ENLIGHT. Transp Res Procedia 2016. https://doi.org/10.1016/j.trpro.2016.05.173.
[5] Feistauer EE, Santos JF, Amancio-Filho ST. A review on direct assembly of through-the-thickness reinforced metal–polymer composite hybrid structures. Polym Eng Sci 2019;59:661–74. https://doi.org/10.1002/pen.25022.
[6] Jahn J, Weber M, Boehner J, Steinhilper R. Assessment Strategies for Composite-metal Joining Technologies-A Review. Procedia CIRP[1] Jahn J, Weber M, Boehner J, Steinhilper R. Assess. Strateg. Compos. Join. Technol. Rev. Procedia CIRP, vol. 50, 2016, p. 689–94. doi10.1016/j.procir.2016.05.034., vol. 50, 2016, p. 689–94. 10.1016/j.procir.2016.05.034.
[7] Sarantinos N, Tsantzalis S, Ucsnik S, Kostopoulos V. Review of through-the-thickness reinforced composites in joints. Compos Struct 2019;229:111404.
[8] Fawcett A, Chen X, Huang X, Li C. Failure analysis of adhesively bonded GFRP/aluminum matrix single composite lap joint with cold worked penetrative reinforcements. Compos Part B Eng 2019;161:96–106. https://doi.org/10.1016/j.compositesb.2018.10.051.
[9] Graham DP, Rezai A, Baker D, Smith PA, Watts JF. The development and scalability of a high strength, damage tolerant, hybrid joining scheme for composite-metal structures. Compos Part A Appl Sci Manuf 2014;64:11–24. https://doi.org/10.1016/j.compositesa.2014.04.018.
[10] Tang H, Liu L. A novel metal-composite joint and its structural performance. Compos Struct 2018;206:33–41. https://doi.org/10.1016/j.compstruct.2018.07.111.
[11] Abe H, Chung JC, Mori T, Hosoi A, Jespersen KM, Kawada H. The effect of nanospike structures on direct bonding strength properties between aluminum and carbon fiber reinforced thermoplastics. Compos Part B Eng 2019;172:26–32. https://doi.org/10.1016/j.compositesb.2019.05.025.
[12] Rezvaninasab M, Farhadinia M, Mirzaei A, Ramzaninezhad M, Khamseh F, Alaei MH. Experimental evaluation of reinforcing the single lap joint in both longitudinal and transverse direction under tensile and bending condition. Int J Adhes Adhes 2019;88:19–25. https://doi.org/10.1016/j.ijadhadh.2018.05.020.
[13] Smith F. Comeld™, an innovation in composite to metal joining. Mater Technol 2005;20:91–6. https://doi.org/10.1080/10667857.2005.11753117.

[14] Ucsnik S, Scheerer M, Zaremba S, Pahr DH. Experimental investigation of a novel hybrid metal-composite joining technology. Compos Part A Appl Sci Manuf 2010; 41:369–74. https://doi.org/10.1016/j.compositesa.2009.11.003.
[15] Parkes PN, Butler R, Meyer J, de Oliveira A. Static strength of metal-composite joints with penetrative reinforcement. Compos Struct 2014;118:250–6. https://doi.org/10.1016/j.compstruct.2014.07.019.
[16] Xiong W, Blackman B, Dear JP, Wang X. The effect of composite orientation on the mechanical properties of hybrid joints strengthened by surfi-sculpt. Compos Struct 2015;134:587–92. https://doi.org/10.1016/j.compstruct.2015.08.083.
[17] Islam MS, Tong L. Influence of pinning on static strength of co-cured metal-GFRP hybrid single lap joints. Compos Part A Appl Sci Manuf 2016;84:196–208. https://doi.org/10.1016/j.compositesa.2016.01.011.
[18] Wang X, Ahn J, Kaboglu C, Yu L, Blackman BRK. Characterisation of composite-titanium alloy hybrid joints using digital image correlation. Compos Struct 2016; 140:702–11. https://doi.org/10.1016/j.compstruct.2015.12.023.
[19] Wang X, Ahn J, Kaboglu C, Yu L, Blackman BRK. Characterisation of composite-titanium alloy hybrid joints using digital image correlation. Compos Struct 2016; 140:702–11. https://doi.org/10.1016/j.compstruct.2015.12.023.
[20] Shang X, Marques EAS, Machado JJM, Carbas RJC, Jiang D, da Silva LFM. Review on techniques to improve the strength of adhesive joints with composite adherends. Compos Part B Eng 2019;177:107363. https://doi.org/10.1016/j.compositesb.2019.107363.
[21] Ramaswamy K, O'Higgins RM, Corbett MC, McCarthy MA, McCarthy CT. Quasi-static and dynamic performance of novel interlocked hybrid metal-composite joints. Compos Struct 2020;253:112769. https://doi.org/10.1016/j.compstruct.2020.112769.
[22] McDonnell P, McGarvey KP, Rochford L, Ó Brádaigh CM. Processing and mechanical properties evaluation of a commingled carbon-fibre/PA-12 composite. Compos - Part A Appl Sci Manuf 2001;32:925–32. https://doi.org/10.1016/S1359-835X(00)00155-X.
[23] Wakeman MD, Zingraff L, Bourban PE, Månson JAE, Blanchard P. Stamp forming of carbon fibre/PA12 composites - A comparison of a reactive impregnation process and a commingled yarn system. Compos Sci Technol 2006;66:19–35. https://doi.org/10.1016/j.compscitech.2005.06.001.
[24] ASTM D 5868. Standard test method for lap shear adhesion for fiber reinforced 39 plastic (FRP) bonding. Standards; 2001. https://doi.org/10.1520/D5868-01R08.2.
[25] Ramaswamy K, O'Higgins RM, Corbett MC, McCarthy CT, McCarthy MA. Experimental study on the performance of hybrid metal-composite joints at quasi-static and intermediate strain rates. In: Proc. ICCM. 22. Melbourne, VIC: ConfEngineers Australia; 2019. p. 2279–87.
[26] da Silva LFM, Öchsner A, Adams RD. Handbook of Adhesion Technology, 53. Berlin, Heidelberg: Springer Berlin Heidelberg; 2011. https://doi.org/10.1007/978-3-642-01169-6.
[27] Corbett MC. Design and optimisation of hybrid composite-metal joints employing novel interlocking faying surface morphology. PhD Thesis, University of Limerick; 2018.
[28] Durante M, Langella A. Bearing behavior of drilled and molded-in holes. Appl Compos Mater 2009. https://doi.org/10.1007/s10443-009-9095-5.
[29] Zitoune R, Crouzeix L, Collombet F, Tamine T, Grunevald YH. Behaviour of composite plates with drilled and moulded hole under tensile load. Compos Struct 2011;93:2384–91. https://doi.org/10.1016/j.compstruct.2011.03.027.
[30] Xu F, Sun L, Zhu L, Yang S, Hui D, Qiu Y. X-ray 3D microscopy analysis of fracture mechanisms for 3D orthogonal woven E-glass/epoxy composites with drilled and moulded-in holes. Compos Part B Eng 2018;133:193–202. https://doi.org/10.1016/j.compositesb.2017.09.033.
[31] Ishikawa T, Amaoka K, Masubuchi Y, Yamamoto T, Yamanaka A, Arai M, et al. Overview of automotive structural composites technology developments in Japan. Compos Sci Technol 2018;155:221–46. https://doi.org/10.1016/j.compscitech.2017.09.015.
[32] Ning H, Lu N, Hassen AA, Chawla K, Selim M, Pillay S. A review of Long fibre thermoplastic (LFT) composites. Int Mater Rev 2020;65:164–88. https://doi.org/10.1080/09506608.2019.1585004.
[33] Alves M, Carlstedt D, Ohlsson F, Asp LE, Pimenta S. Ultra-strong and stiff randomly-oriented discontinuous composites: closing the gap to quasi-isotropic continuous-fibre laminates. Compos Part A 2020;132:105826. https://doi.org/10.1016/j.compositesa.2020.105826.
[34] Saleema N, Sarkar DK, Paynter RW, Gallant D, Eskandarian M. A simple surface treatment and characterization of AA 6061 aluminum alloy surface for adhesive bonding applications. Appl Surf Sci 2012;261:742–8. https://doi.org/10.1016/j.apsusc.2012.08.091.
[35] Ramaswamy K, O'Higgins RM, Kadiyala AK, McCarthy MA, McCarthy CT. Evaluation of grit-blasting as a pre-treatment for carbon-fibre thermoplastic composite to aluminium bonded joints tested at static and dynamic loading rates. Compos Part B Eng 2020;185:107765. https://doi.org/10.1016/j.compositesb.2020.107765.
[36] Dow Automotive. Dow automotive product overview, betamate body structural adhesive; 2018.
[37] Hart-Smith LJ. Analysis and design of advanced composite bonded joints. NASA Contract Reports 1974.
[38] da Silva LFM, Carbas RJC, Critchlow GW, Figueiredo MAV, Brown K. Effect of material, geometry, surface treatment and environment on the shear strength of single 40 lap joints. Int J Adhes Adhes 2009;29:621–32. https://doi.org/10.1016/j.ijadhadh.2009.02.012.
[39] Karachalios EF, Adams RD, da Silva LFM. Single lap joints loaded in tension with high strength steel adherends. Int J Adhes Adhes 2013;43:81–95. https://doi.org/10.1016/j.ijadhadh.2013.01.016.
[40] Banea MD, da Silva LFM, Carbas R, Campilho RDSG. Effect of material on the mechanical behaviour of adhesive joints for the automotive industry. J Adhes Sci Technol 2017;31:663–76. https://doi.org/10.1080/01694243.2016.1229842.
[41] Bamberg PAMGP, Schiebahn A, Marx B, Reisgen U, Coelho RS, Barbosa JDV. Digital image correlation analysis of the effects of the overlap length, adhesive thickness and adherends yield strength over similar and dissimilar joints of high strength steel and aluminum alloys. Int J Adhes Adhes 2018;83:69–75. https://doi.org/10.1016/j.ijadhadh.2018.02.010.
[42] Banea MD. Influence of adherend properties on the strength of adhesively bonded joints. MRS Bull 2019;44:625–9. https://doi.org/10.1557/mrs.2019.180.
[43] Mouritz AP. Review of z-pinned composite laminates. Compos Part A Appl Sci Manuf 2007;38:2383–97. https://doi.org/10.1016/j.compositesa.2007.08.016.
[44] Chang P, Mouritz AP, Cox BN. Properties and failure mechanisms of pinned composite lap joints in monotonic and cyclic tension. Compos Sci Technol 2006;66: 2163–76. https://doi.org/10.1016/j.compscitech.2005.11.039.
[45] ASTM D5573-99(2005). Standard practice for classifying failure mode in fiber-reinforced-plastic (FRP). ASTM B Stand; 2005. https://doi.org/10.1520/D5573-99R12.2.
[46] Cox BN. Snubbing Effects in the Pullout of a Fibrous Rod from a Laminate. Mech Adv Mater Struct 2005;12:85–98. https://doi.org/10.1080/15376490490493899.
[47] Morin D, Haugou G, Lauro F, Bennani B, Bourel B. Elasto-viscoplasticity Behaviour of a Structural Adhesive Under Compression Loadings at Low, Moderate and High Strain Rates. J Dyn Behav Mater 2015;1:124–35. https://doi.org/10.1007/s40870-015-0010-x.
[48] Pouriayevali H, Arabnejad S, Guo YB, Shim VPW. A constitutive description of the rate-sensitive response of semi-crystalline polymers. Int J Impact Eng 2013;62: 35–47. https://doi.org/10.1016/j.ijimpeng.2013.05.002.
[49] Koh TM, Feih S, Mouritz AP. Strengthening mechanics of thin and thick composite T-joints reinforced with z-pins. Compos Part A Appl Sci Manuf 2012;43:1308–17. https://doi.org/10.1016/j.compositesa.2012.03.023.
[50] Nanayakkara AM, Feih S, Mouritz AP. Improving the fracture resistance of sandwich composite T-joints by z-pinning. Compos Struct 2013;96:207–15.
[51] Li M, Chen P. A new FE model for predicting the bridging micromechanisms of a Z-pin. Compos Struct 2019;223:110957.
[52] May M, Hesebeck O, Marzi S, Böhme W, Lienhard J, Kilchert S, et al. Rate dependent behavior of crash-optimized adhesives – Experimental characterization, model development, and simulation. Eng Fract Mech 2015;133:112–37.